Iverson, R. M. & George, D. L. (2016). *Géotechnique* **66**, No. 3, 175–187 [http://dx.doi.org/10.1680/jgeot.15.LM.004]

# Modelling landslide liquefaction, mobility bifurcation and the dynamics of the 2014 Oso disaster

R. M. IVERSON* and D. L. GEORGE*

Some landslides move slowly or intermittently downslope, but others liquefy during the early stages of motion, leading to runaway acceleration and high-speed runout across low-relief terrain. Mechanisms responsible for this disparate behaviour are represented in a two-phase, depth-integrated, landslide dynamics model that melds principles from soil mechanics, granular mechanics and fluid mechanics. The model assumes that gradually increasing pore-water pressure causes slope failure to nucleate at the weakest point on a basal slip surface in a statically balanced mass. Failure then spreads to adjacent regions as a result of momentum exchange. Liquefaction is contingent on pore-pressure feedback that depends on the initial soil state. The importance of this feedback is illustrated by using the model to study the dynamics of a disastrous landslide that occurred near Oso, Washington, USA, on 22 March 2014. Alternative simulations of the event reveal the pronounced effects of a landslide mobility bifurcation that occurs if the initial void ratio of water-saturated soil equals the lithostatic, critical-state void ratio. They also show that the tendency for bifurcation increases as the soil permeability decreases. The bifurcation implies that it can be difficult to discriminate conditions that favour slow landsliding from those that favour liquefaction and long runout.

KEYWORDS: dynamics; landslides; liquefaction; numerical modelling; pore pressure

## INTRODUCTION

Many landslides never attain speeds as large as 0·1 m/s, but others transform into highly mobile flows that reach speeds greater than 10 m/s and travel long distances across flat or gently sloping terrain. Field evidence and laboratory experiments indicate that this high mobility commonly results from partial or complete liquefaction of water-laden landslide material or overridden bed material, and that liquefaction is caused by some combination of undrained compression and contractive shearing of one or both of these materials (e.g. Hutchinson & Bhandari, 1971; Bishop, 1973; Eckersley, 1990; Iverson *et al*., 1997, 2000, 2011; Spence & Guymer, 1997; Wang & Sassa, 2001, 2003; Hungr & Evans, 2004; Ochiai *et al*., 2007). Diverse terms such as 'flowslide', 'debris flow', 'mudflow', 'mudslide', or 'debris avalanche' have been used to describe landslides that liquefy wholly or partially. Irrespective of differences in terminology, all liquefying landslides exhibit a pronounced reduction of frictional strength following the onset of landslide motion, a persistence of low friction during at least part of the landslide runout process and a recovery of frictional strength during post-depositional consolidation of landslide debris.

The evolution of material strength in a landslide that liquefies is contingent on the evolving dynamics of the landslide as a whole. Therefore, realistic models of liquefying landslides cannot be founded on traditional rheological formulas, which specify that local resistance to motion is a function of only local stress states and displacements or displacement rates (Iverson, 2003). Instead, realistic models must allow the apparent rheology to evolve in response to feedbacks that develop as the distributions of landslide mass, momentum and pore pressure evolve. These large-scale feedbacks can cause time- and space-dependent changes in the local material state, similar to changes that play a central role in quasi-static, critical-state soil mechanics (e.g. Schofield & Wroth, 1968; Wood, 1990). In contrast to evolving material states in quasi-static soils, however, evolving material states in liquefying landslides may be influenced by arbitrarily large, rapid displacements and momentum transfer.

Models that aim to explain the behaviour of landslides that liquefy must also be able to explain landslide behaviour in which liquefaction does not occur – without invoking differences in intrinsic granular friction. Models that lack this discriminatory power can shed no light on factors favouring or limiting the potential for liquefaction and attendant high mobility. Indeed, the difference between relatively slow, stable landslide motion and unstable, liquefying landslide motion may represent a sharp behavioural bifurcation (Iverson *et al*., 2000; Iverson, 2005). Important questions about such a bifurcation concern its sensitivity to initial conditions and material properties.

This paper summarises the conceptual and mathematical framework, as well as practical application, of a recently developed computational model that simulates bifurcating landslide dynamics without invoking any changes in intrinsic friction. Instead, changes in effective friction arise from feedbacks that depend mostly on the initial void ratio of water-saturated soil and on the relative timescales for gravity-driven landslide motion and relaxation of excess pore-water pressure that is generated by that motion. These feedbacks determine the propensity for liquefaction and high mobility. The model is used to study the dynamics of a disastrous, highly mobile landslide that occurred on 22 March 2014 near the community of Oso in Washington State, USA (Fig. 1).

## MODEL FRAMEWORK

### *Conceptual background*

The proposed model, called D-Claw, considers the gravity-driven motion of fluid-filled granular mixtures that can undergo dilation and contraction during both quasi-static and inertial deformation. The model employs depth-integrated continuum mechanical equations that blend

Manuscript received 8 February 2015; revised manuscript accepted 25 June 2015. Published online ahead of print 30 September 2015. Discussion on this paper closes on 1 August 2016, for further details see p. ii.

* U.S. Geological Survey, Vancouver, Washington, USA.

**Fig. 1. West-looking oblique aerial photograph of the 22 March 2014 Oso landslide source area and deposit as they appeared on 7 May 2014. See Iverson *et al.* (2015) for further details. Photograph courtesy of Vaughn Collins, Northwest Hydraulic Consultants**

concepts from critical-state soil mechanics, fluid mechanics and granular mechanics. Iverson & George (2014) provide a comprehensive derivation of the model equations, and George & Iverson (2014) describe the numerical method of solving the equations, as well as tests of model predictions against data from large-scale experiments. Here the model's key attributes are summarised.

The mathematical structure and numerical solution technique used by D-Claw permit seamless simulation of landslide motion from initiation to deposition. For statically balanced initial states, the D-Claw equations take a familiar form, because they reduce to force-balance equations similar to those used in three-dimensional (3D) limit-equilibrium slope-stability analyses that employ methods of columns. Modelled landslide motion is triggered by specifying a gradual growth of basal pore-water pressure. Use of statically balanced initial states distinguishes D-Claw from landslide dynamics models that use dam-break initial conditions and thereby impose a finite initial force imbalance (e.g. Hungr, 1995).

Depth integration embeds the effects of evolving surface and basal boundary conditions into the governing conservation equations used in D-Claw. Depth integration also reduces the degrees of freedom in the conservation equations, thereby facilitating efficient computation of solutions. This reduction requires approximation of the vertical or bed-normal momentum equation by a static force balance – an approximation that is justified by scaling if a landslide's length and width greatly exceeds its thickness (Savage & Hutter, 1989). Such scaling is not applicable in all landslides, but the depth-integrated form of D-Claw nevertheless provides a useful compromise between generality and practicality. Moreover, solutions of the depth-integrated equations yield predictions that can be rigorously tested, because they produce output with a resolution similar to that of data obtained in large-scale landslide dynamics experiments (George & Iverson, 2014).

D-Claw employs a dilatancy angle, $\psi$, to help link continuum-scale dynamics to grain-scale behaviour. The model does not specify values of $\psi$, but instead calculates them by using the difference between the ambient solid volume fraction $m$ and an equilibrium solid volume fraction $m_{eq}$ that varies in response to changes in the local stress state and shear rate. (Note that values of $m$ are related to those of the porosity $n$ and void ratio $e$ by $m = 1 - n = 1/(1 + e)$.) Thus, the D-Claw dilatancy definition

$$\tan \psi = m - m_{eq} \tag{1}$$

accounts for the fact that values of both $m$ and $m_{eq}$ evolve. However, the equilibrium value $m_{eq}$ responds instantaneously to changes in the local material state, while the ambient value $m$ relaxes gradually toward $m_{eq}$ with a timescale that is determined by coupled evolution equations (Iverson & George, 2014).

Values of $m_{eq}$ in D-Claw are constrained by the results of annular shear cell experiments with concentrated mixtures of grains and liquids (Boyer *et al.*, 2011). These experiments allowed unrestricted coevolution of $m$ and the shear rate $\dot{\gamma}$ under drained, stress-controlled conditions, which ultimately led to steady equilibrium states described by

$$m_{eq}(N) = \frac{m_{crit}}{1 + \sqrt{N}} \tag{2}$$

Here $m_{crit}$ is the value of $m_{eq}$ that applies if $\dot{\gamma} = 0$ and the stress state is lithostatic, and $N$ is the dimensionless ratio of viscous shear stresses and grain-contact normal stresses, which is zero in static states and finite if $\dot{\gamma} \neq 0$. In D-Claw, $N$ serves as a scalar measure of the local material state, and it is defined mathematically as

$$N = \frac{\mu \dot{\gamma}}{\sigma_e + \rho_s \dot{\gamma}^2 \delta^2} \tag{3}$$

where $\mu$ is the pore-fluid viscosity, $\sigma_e$ is the ambient mean effective normal stress, $\rho_s$ is the mass density of solid grains and $\delta$ is a characteristic grain diameter. The quantity $\rho_s \dot{\gamma}^2 \delta^2$ in the denominator of equation (3) gauges the inertial contribution to grain-contact stresses (cf. Bagnold, 1954), and it serves to keep $N$ finite in fully liquefied states with $\sigma_e = 0$. However, $\sigma_e \gg \rho_s \dot{\gamma}^2 \delta^2$ applies in most instances owing to the relaxation of $m$ toward $m_{eq}$ and the accompanying relaxation of excess pore-fluid pressure. As a result, equation (3) is typically approximated well by the form $N = \mu \dot{\gamma}/\sigma_e$ utilised by Boyer *et al.* (2011), and the practical full-scale range of $N$ is $0 \leq N \leq 1$ (Iverson & George, 2014).

Evolution of $m$ influences the evolution of several other key quantities in D-Claw. For example, the mixture bulk density, $\rho$, is defined by

$$\rho = \rho_s m + \rho_f (1 - m) \tag{4}$$

where $m$ evolves but both $\rho_s$ and the fluid mass density $\rho_f$ are treated as constants. In turn, the evolution of $\rho$ influences the mixture's linear momentum, defined as $\rho \boldsymbol{v} = \rho_s m \boldsymbol{v}_s + \rho_f (1 - m) \boldsymbol{v}_f$, where $\boldsymbol{v}_s$ is the solid-phase velocity, $\boldsymbol{v}_f$ is the fluid-phase velocity and $\boldsymbol{v}$ is the velocity of the mixture. This momentum definition implies that the mixture velocity is defined by

$$\boldsymbol{v} = \frac{\rho_s m \boldsymbol{v}_s + \rho_f (1 - m) \boldsymbol{v}_f}{\rho} \tag{5}$$

Another velocity linked to evolution of $m$ is the apparent velocity (i.e. volume flux per unit area) of the fluid phase relative to the solid phase, $\boldsymbol{q}$, defined as

$$\boldsymbol{q} = (1 - m)(\boldsymbol{v}_f - \boldsymbol{v}_s) \tag{6}$$

Although $q$ does not appear explicitly in the D-Claw equations, it plays an important role in calculating solid–fluid drag. D-Claw evaluates this drag by employing Darcy's law

$$\boldsymbol{q} = -\frac{k(m)}{\mu}\nabla p_e \tag{7}$$

which applies in a frame of reference that translates with the solid velocity, $\boldsymbol{v}_s$ (Bear, 1972). In equation (7) $p_e$ is the excess pore-fluid pressure (i.e. the deviation from hydrostatic pressure), and $k(m) = k_0 \exp[(m_0 - m)/0{\cdot}04]$ is an empirically constrained intrinsic hydraulic permeability that increases as $m$ decreases (Iverson & George, 2014). The initial value of $k$ is $k_0$, which applies in an initial static state with $m = m_0$. The parameter $k_0$ has SI units of $m^2$, and is related to the hydraulic conductivity $K$ by $k = (K\mu)/(\rho_f g)$, where $K$ has SI units of m/s. Values $k_0 \leq 10^{-7}\,m^2$ are applicable for static earth materials composed mostly of grains that are gravel-sized or smaller (Freeze & Cherry, 1979), but values of $k$ for rapidly deforming granular materials could be a few orders of magnitude larger.

Taken together, equation (4) through equation (7) with $k < 10^{-3}\,m^2$ imply that $\boldsymbol{v} \approx \boldsymbol{v}_s$ is generally a good approximation for most landslides, and D-Claw exploits this fact to use $\boldsymbol{v}_s$ as a surrogate for $\boldsymbol{v}$. As shown by Iverson & George (2014), the approximation $\boldsymbol{v} \approx \boldsymbol{v}_s$ is mathematically rigorous if $\|\boldsymbol{q}\|/\|\boldsymbol{v}_s\| \ll 1$ is satisfied or if the landslide material is quasi-static and $\|\boldsymbol{q}\| \ll 0{\cdot}1$ m/s is satisfied (where $\|\|$ denotes the Euclidean norm of a vector). The approximation $\boldsymbol{v} \approx \boldsymbol{v}_s$ allows D-Claw to account for the chief effects of solid–fluid interactions while computing a single velocity field, thereby conferring desirable mathematical properties (George & Iverson, 2014).

A final constitutive parameter linked to the evolving value of $m$ in D-Claw is the bulk volumetric compressibility of the solid–fluid mixture, $\alpha$. To evaluate this compressibility, D-Claw uses the empiricism

$$\alpha = \frac{a}{m(\sigma_e + \sigma_0)} \tag{8}$$

where $a$ is a proportionality coefficient and $\sigma_0$ is a reference normal stress that establishes the maximum compressibility, $a/m\sigma_0$, which applies if $\sigma_e = 0$. On the basis of fits to experimental data for liquefied and partially liquefied sediment–water mixtures, suitable values of $a$ and $\sigma_0$ are generally $a \approx 0{\cdot}03$ and $\sigma_0 \approx 1$ kPa (Iverson & George, 2014).

*Governing equations*

D-Claw utilises depth-integrated Cartesian components of $\boldsymbol{v}$, which are $u$, $v$ and $w$ in the $x$, $y$ and $z$ directions, respectively (Fig. 2). Depending on the problem of interest, $z$ may be oriented vertically or inclined so that it is normal to a basal surface, but in all cases $x$ and $y$ are normal to $z$ (cf. George & Iverson, 2014). Depth integration extends from a fixed basal surface at $z = b(x, y)$ to the evolving landslide upper surface at $z = \eta(x, y, t)$, such that the landslide thickness is given by $h(x, y, t) = \eta - b$. D-Claw computes the velocity components $u(x, y, t)$ and $v(x, y, t)$ explicitly, but it treats $w(x, y, t)$ as an implicit variable that is related to $u(x, y, t)$, $v(x, y, t)$ and $h(x, y, t)$ through kinematic boundary conditions. These conditions stipulate that no mass passes through the upper or basal surfaces of the landslide (Iverson & George, 2014). More general kinematic boundary conditions and associated jump conditions apply if entrainment or deposition of material occurs at these surfaces (Iverson & Ouyang, 2015).

In addition to $u(x, y, t)$, $v(x, y, t)$ and $h(x, y, t)$, D-Claw computes $m(x, y, t)$ and the basal pore-fluid pressure, $p_b(x, y, t)$. The mass-, momentum- and pore-pressure

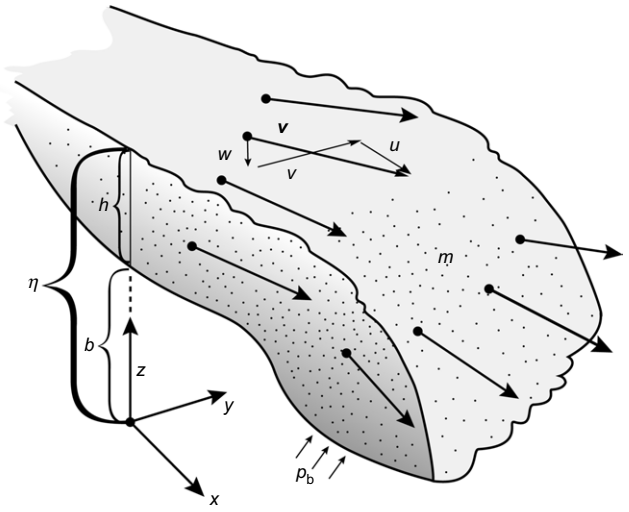


**Fig. 2. Schematic illustration of the coordinate system and depth-averaged dependent variables $u(x, y, t)$, $v(x, y, t)$, $h(x, y, t)$, $m(x, y, t)$ and $p_b(x, y, t)$ used in D-Claw calculations of the behaviour of the 2014 Oso landslide**

conservation equations governing coupled evolution of these variables may be written as (Iverson & George, 2014; George & Iverson, 2014)

$$\frac{\partial h}{\partial t} + \frac{\partial (hu)}{\partial x} + \frac{\partial (hv)}{\partial y} = \frac{\rho - \rho_f}{\rho} D \tag{9}$$

$$\frac{\partial (hm)}{\partial t} + \frac{\partial (hum)}{\partial x} + \frac{\partial (hvm)}{\partial y} = -\frac{\rho_f}{\rho} Dm \tag{10}$$

$$\begin{aligned}\frac{\partial (hu)}{\partial t} + \frac{\partial (hu^2)}{\partial x} + \frac{\partial (huv)}{\partial y} + \kappa \frac{\partial}{\partial x}\left(\frac{1}{2} g_z h^2\right) \\ + \frac{h(1-\kappa)}{\rho}\frac{\partial p_b}{\partial x} = g_x h - \frac{\tau_{zx}}{\rho} + \frac{\rho - \rho_f}{\rho} Du\end{aligned} \tag{11}$$

$$\begin{aligned}\frac{\partial (hv)}{\partial t} + \frac{\partial (hv^2)}{\partial y} + \frac{\partial (hvu)}{\partial x} + \kappa \frac{\partial}{\partial y}\left(\frac{1}{2} g_z h^2\right) \\ + \frac{h(1-\kappa)}{\rho}\frac{\partial p_b}{\partial y} = g_y h - \frac{\tau_{zy}}{\rho} + \frac{\rho - \rho_f}{\rho} Dv\end{aligned} \tag{12}$$

$$\begin{aligned}\frac{\partial p_b}{\partial t} + u\frac{\partial p_b}{\partial x} + v\frac{\partial p_b}{\partial y} + \frac{(3\rho + \rho_f) g_z h}{4}\left(\frac{\partial u}{\partial x} + \frac{\partial v}{\partial y}\right) \\ - \rho_f g_z D\left(\frac{\rho - \rho_f}{4\rho}\right) = -\frac{3k}{\alpha\mu h^2}[p_b - \rho_f g_z h] \\ - \left(\frac{3\sqrt{u^2 + v^2}}{\alpha h}\right)\tan\psi\end{aligned} \tag{13}$$

in which $g_x$, $g_y$ and $g_z$ are components of the gravitational acceleration vector, and

$$D \equiv \int_b^\eta (\nabla \cdot \boldsymbol{v}_s)\,dz = -\frac{h}{m}\left(\frac{\partial m}{\partial t} + u\frac{\partial m}{\partial x} + v\frac{\partial m}{\partial y}\right) \tag{14}$$

is the depth-integrated granular dilation rate. Like the dependent variables in equations (9) through (13), $D$ is a function of $x$, $y$ and $t$. It appears in the source terms of equations (9) through (13), and it compensates for the absence of derivatives of $\rho$ in the equations. D-Claw isolates the influence of $D$ because of the important effect of the

dilation rate in regulating landslide motion influenced by pore-pressure feedback.

Another key feature of equations (9) through (13) is that $h$ is defined such that $\rho h(x, y, t)$ is the landslide mass per unit basal area $\Delta x \Delta y$ (Iverson & George, 2014). As a consequence, $z = \eta = b + h$ denotes the height of a *virtual free surface* that may not precisely match the height of either the granular solid surface or pore-fluid surface (Fig. 3). This definition of $h$ is necessary in order to ensure mass conservation, because pore fluid moves with respect to adjacent solid grains in response or dilation or contraction, such that $\nabla \cdot \boldsymbol{v}_s = -\nabla \cdot \boldsymbol{q}$ is satisfied. During this process the fluid level falls or rises relative to the level of grains at the landslide surface.

Iverson & George (2014) also show that the definition of the virtual free surface lends additional meaning to the depth-integrated dilation rate $D$, because the $z$ component of $\boldsymbol{q}$ at $z = \eta = b + h$ locally satisfies $-q_z|_{z=\eta} = D$ as fluid passes through the virtual free surface. Iverson & George (2014) relate $q_z|_{z=\eta}$ and $D$ to $k/\mu$ by employing Darcy's law, equation (7), and by deducing that the evolving bed-normal pore-pressure profiles $p(z, t)$ can be approximated by a series of steady-state profiles that are constrained by mass conservation, by boundary conditions and by scaling considerations which imply that $\left|\partial^2 p/\partial z^2\right| \gg \left|\partial^2 p/\partial x^2\right|, \left|\partial^2 p/\partial y^2\right|$ (Fig. 4). The resulting equation

$$D = -\frac{2k}{\mu h}(p_b - \rho_f g_z h) \tag{15}$$

helps provide closure to equations (9) through (13) by explicitly linking evolution of $D$ to evolution of $h$ and $p_b$. It also implies that $p_b = \rho_f g_z h$ is satisfied in the absence of dilation or contraction.

The momentum-conservation equations (11) and (12) contain three as-yet undefined quantities, $\tau_{zx}$, $\tau_{zy}$ and $\kappa$, which account for the depth-integrated effects of stresses. The basal shear tractions, $\tau_{zx}$ and $\tau_{zy}$ apply at $z = b$ and summarise stress contributions due to solid-phase Coulomb friction and fluid-phase viscous shearing. In D-Claw these tractions are specified by

$$\tau_{zx} = [\rho g_z h - p_b] \tan(\phi + \psi) \frac{u}{(u^2 + v^2)^{1/2}} + 2\mu(1 - m)\frac{u}{h} \tag{16}$$

$$\tau_{zy} = [\rho g_z h - p_b] \tan(\phi + \psi) \frac{v}{(u^2 + v^2)^{1/2}} + 2\mu(1 - m)\frac{v}{h} \tag{17}$$

where $\rho g_z h - p_b$ is the basal effective normal stress, and $\phi + \psi$ is the total basal friction angle, which accounts for the contributions of a fixed, constant-volume friction angle, $\phi$, and for those of the evolving dilatancy angle, $\psi$. The factors $u/(u^2 + v^2)^{1/2}$ and $v/(u^2 + v^2)^{1/2}$ are included in equations (16) and (17) to ensure that positive Coulomb tractions resist positive velocities. In the viscous (i.e. final) terms of equations (16) and (17), $2u/h$ and $2v/h$ provide depth-integrated estimates of the $x$ and $y$ components of the shear rate, $\dot{\gamma}$. In general, these viscous terms are much smaller than the Coulomb friction terms, except in atypical circumstances in which the basal effective normal stress nearly vanishes (i.e. $\rho g_z h - p_b \approx 0$).

The other stress-related quantity in equations (11) and (12) is the lateral normal stress coefficient, $\kappa$. Building on the work of Savage & Hutter (1989), many depth-integrated landslide-dynamics models have used expressions for $\kappa$ that are derived from variants of Rankine earth-pressure theory. This approach requires specification of additional parameter values, however (e.g. Iverson & Denlinger, 2001; McDougall & Hungr, 2004). D-Claw includes the option of using this approach, but to obtain the model results reported here, the simple idealisation $\kappa = 1$ suggested by findings of Gray *et al.*

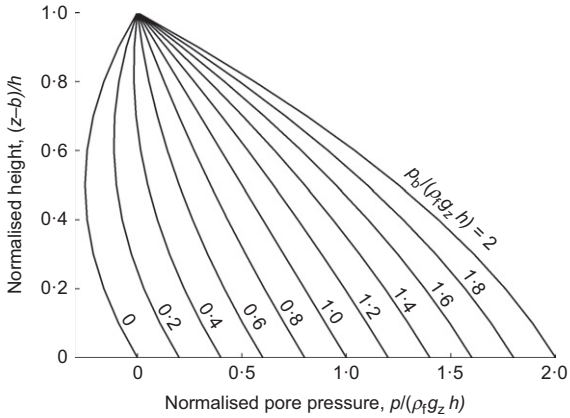


**Fig. 4. Graph illustrating a sequence of instantaneous, steady-state pore-pressure profiles that satisfy $\partial^2 p/\partial z^2 =$ constant and the boundary conditions, $(\partial p/\partial z)|_{z=b} = 0$ and $p|_{z=b+h} = 0$ as the normalised basal pore pressure $p_b/(\rho_f g_z h)$ evolves. As $p_b/(\rho_f g_z h) \to 0$, pore pressures become negative at heights $b < z < b + h$, implying the existence of a tension-saturated state. For further details see Iverson & George (2014)**

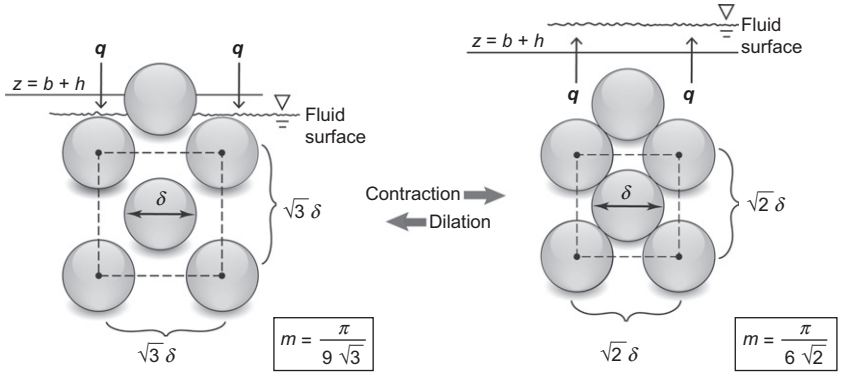


**Fig. 3. Schematic illustration of the change in the position of the virtual free surface at $z = \eta = b + h$ in response to dilation or contraction of a mixture with $\rho_s/\rho_f = 2{\cdot}7$. Dashed lines indicate 2D boundaries of isometric 3D unit cells used to calculate the solid volume fraction, $m$. For illustrative purposes, solid grains are assumed to be identical spheres with diameter $\delta$, and sphere centre spacings are chosen as either $\sqrt{3}\delta$ or $\sqrt{2}\delta$. Spheres do not contact one another in either the dilated or contracted state illustrated here. A flux of pore fluid ($q$) through the virtual free surface accompanies changes in $m$ caused by dilation or contraction. The idealised geometries used in this illustration exaggerate changes in $m$, $q$ and $h$ relative to changes that would occur in landslide materials containing grains with diverse shapes and sizes**

(1999, 2003) is employed. Use of this idealisation helps focus the simulations on the phenomena of principle interest: pore-pressure feedback and the causes and effects of landslide liquefaction.

*Interpretation of the pore-pressure evolution equation (13)*

Among the D-Claw equations, equation (13) has the most unconventional form, and it merits some explanation because it plays a pivotal role in the model. As detailed by Iverson & George (2014), the equation is derived by assuming that $\nabla \cdot \boldsymbol{v}_s$ and $\nabla \cdot \boldsymbol{q}$ are not functions of $z$ (consistent with the assumption that $m$ and $D$ are not functions of $z$), thereby linking the evolving basal pore pressure $p_b$ to the pore-pressure distributions in overlying material (Fig. 4). The first term in equation (13) accounts for the temporal evolution of $p_b$, and the next two terms account for advective transport of $p_b$ by the velocity components $u$ and $v$. The final two terms on the left-hand side of equation (13) account for changes in $p_b$ that result from evolution of $h$ and $m$. (As shown by Iverson & George (2014), these terms can be recast by including total time derivatives of $h$ and $\rho$ in the equation.) The first term on the right-hand side of equation (13) accounts for relaxation of $p_b$ toward the hydrostatic equilibrium pressure $\rho_f g_z h$. The reciprocal of the coefficient $3k/\alpha\mu h^2$ in this term can be interpreted as a pore-pressure relaxation timescale, and contained within this timescale is the parameter group $k/\alpha\mu$, which can be interpreted as a pore-pressure diffusivity or consolidation coefficient. The final term in equation (13) accounts for the role of shear-driven contraction or dilation in causing growth or decline of pore pressure.

Iverson & George (2014) show that a lowest-order, steady-state approximation of equation (13) reduces the equation to a simple balance involving only the pore-pressure production and relaxation terms on the right-hand side. This balance can be expressed as

$$p_b - \rho_f g_z h = -\frac{\mu h}{k}(u^2 + v^2)^{1/2} \tan \psi \qquad (18)$$

If a constant value $\psi < 0$ applies, then the steady state defined by equation (18) indicates that pore-space contraction produces pore-fluid pressures that are larger than hydrostatic. Fast shearing, represented by large values of $(u^2 + v^2)^{1/2}$, enhances this production, whereas high permeability, represented by large values of $k$, reduces it. By contrast, if a constant value $\psi > 0$ applies, then shear-induced dilation of pore space reduces the pore-fluid pressure to values less than hydrostatic. This simple steady-state view of pore-pressure responses aids interpretation of the computational results – although the dynamics represented in equations (9) through (13) are intrinsically time-dependent and are influenced by evolving $\psi$ values.

*Mathematical properties and numerical implementation*

An important mathematical attribute of the governing equations (9) through (13) is that they form a fully hyperbolic system with desirable stability properties (George & Iverson, 2014). The equations' hyperbolicity is due, in part, to the fact that they model only a single velocity field, rather than separate velocity fields for the solid and fluid phases. Many two-phase depth-averaged models are known to lose hyperbolicity when solid and fluid velocity fields diverge past some threshold (e.g. Pitman & Le, 2005). This behaviour can render the governing equations unstable, and the loss of hyperbolicity must be prevented numerically, commonly through techniques that limit the differences between solid and fluid velocity fields.

The numerical schemes implemented in D-Claw employ shock-capturing finite-volume methods based on wave-propagation algorithms, which utilise solutions to Riemann problems at grid cell interfaces for numerical updates (LeVeque, 2002). This highly developed family of numerical schemes is implemented in the open-source software package Clawpack (Clawpack, 2015). A specialised version of Clawpack, called GeoClaw, is designed to address phenomena common to shallow flow problems. D-Claw is an extension of GeoClaw developed specifically for solving the equations utilised here (George & Iverson, 2014).

A significant and well-known challenge in using wave-propagation methods to simulate shallow flows across topography involves preservation of balanced steady states (e.g. Bale *et al.*, 2002). In landslide dynamics calculations, such steady states play a crucial role, because virtually all landslides begin from statically balanced initial states and also conclude in statically balanced states (George & Iverson, 2014). In D-Claw the preservation of steady states is accomplished with an adaptation of well-balanced methods developed previously for shallow-water flow problems (Bale *et al.*, 2002; George, 2008). With this approach, the frictional resistance terms that balance gravitational driving forces in steady states are incorporated directly in a specially designed Riemann solver (George, 2008; George & Iverson, 2014). This methodology also ensures that landslide dynamics involving small deviations from a balanced steady state are computed without introducing spurious numerical instabilities.

Another major computational challenge stems from the need for high spatial resolution of solutions in regions where values of variables change abruptly, as at the propagating fronts of landslides. On the other hand, high resolution can greatly increase computation time if it is maintained everywhere in the solution domain. To attain high resolution as well as high computational efficiency, D-Claw uses adaptive mesh refinement (AMR) tailored to shallow flow problems with variable topography (LeVeque *et al.*, 2011). George & Iverson (2014) summarise the present implementation of AMR and provide references to more detailed literature on the topic. As a result of D-Claw's use of AMR, none of the alternative simulations of the Oso landslide required more than 40 min of CPU time on an ordinary desktop computer with a 2·67 GHz processor. At the same time, they took full advantage of the 0·91 m horizontal resolution of lidar-derived digital elevation models of the topography of the site.

## MODELLING THE DYNAMICS OF THE OSO LANDSLIDE

D-Claw is used to study the dynamics of a large, high-mobility landslide that occurred following a long period of unusually wet weather near Oso, Washington, USA, on 22 March 2014 (Fig. 1). The landslide (officially named the SR 530 landslide by Washington State) caused 43 fatalities, ranking it second only to a 1985 event in Mameyes, Puerto Rico, as the worst landslide disaster in US history (cf. Jibson, 1992). Results of a multidisciplinary investigation of the landslide's behaviour are presented elsewhere (Iverson *et al.*, 2015). Here the focus is placed on insights that can be gained from using D-Claw to model the dynamics of the landslide as well as a spectrum of alternative behaviours computed for landslides with the same initial geometry and basal friction angle, but with modified values of the initial solid volume fraction $m_0$ and permeability $k_0$.

*Constraints from observations*

Constraints on the character of the Oso landslide are provided by pre-event (2013) and post-event (2014) lidar

topography, geological mapping, precipitation records, eyewitness observations, broadband seismic recordings and post-event field investigations (Iverson *et al.*, 2015). The landslide originated on a 180-m high riverside bluff that was inclined $<20°$ on average and composed of horizontally bedded proglacial and glacial sediments, ranging from a glaciolacustrine silt-and-clay unit at the base of the slope to a glaciofluvial sand-rich unit at the top (Dragovich *et al.*, 2003). A mantle of colluvium deposited during previous episodes of landsliding at the site covered these sediments on much of the lower part of the slope and also covered a small part of the adjacent river floodplain. Investigations of the detailed stratigraphy and geotechnical properties of the 2014 landslide source materials are underway but have not been completed. Therefore, the present modelling assumes homogeneous landslide source material with properties typical of poorly sorted sandy sediment.

The post-event topography and boundaries of the primary depositional units of the 2014 landslide are illustrated in Fig. 5. The uppermost part of the landslide mass remained stranded in the source area as a relatively coherent slump block. Downslope of this block, most of the landslide deposit consisted of hummocky, disaggregated debris-avalanche material $> 5$ m thick. Scattered amid the hummocks were pools of sediment that remained partially liquefied for weeks following the event. The distal margin of the deposit consisted of fully liquefied, wood-freighted debris-flow material, which in most places formed a veneer $<0{\cdot}3$ m thick overlying debris-avalanche material. On the basis of these variegated deposits, Iverson *et al.* (2015) described the landslide as a debris avalanche flow, but the term 'flowslide' may also be appropriate.

Eyewitness accounts, broadband seismicity radiated by the landslide and the character of the landslide deposits are consistent with the interpretation that the event involved three key stages of motion (Iverson *et al.*, 2015). First, only a lower portion of the landslide moved, and it likely displaced the colluvium left on the slope by prior episodes of landsliding as well as some of the underlying, bedded sediments. This stage of motion lasted about 50 s, but it did not produce a high-mobility landslide. As the first stage of landsliding decelerated, a second stage developed. It involved abrupt, retrogressive collapse of the debuttressed upslope bluff, which likely caused undrained loading of the already unstable material downslope. A high-speed, partially liquefied landslide ensued, and it violently impacted the adjacent North Fork Sillaguamish River. The third stage of motion involved displacement or entrainment of as much as 50 000 $m^3$ of river water, which facilitated development of a water-rich debris flow at the leading edge of the landslide. The debris-flow volume was relatively modest (about 200 000 $m^3$), but the debris flow was pushed across the adjacent 1-km-wide floodplain by the much larger debris avalanche behind it. The duration of associated high-frequency ground shaking indicates that the high-energy stage of landslide motion lasted about 100 s (Iverson *et al.*, 2015).

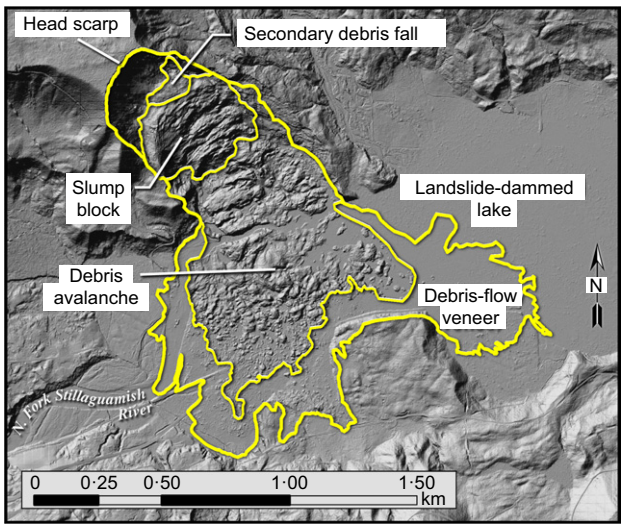


**Fig. 5. Shaded relief lidar image of the 22 March 2014 Oso landslide, Washington State, USA (latitude 48·280°N, longitude 121·844°W). The thick pale line (yellow online) denotes the perimeter of the landslide path, and thinner pale lines denote boundaries of major depositional units delineated by Iverson *et al.* (2015)**

Estimation of the total volume of the Oso landslide required differencing the 2013 and 2014 lidar topography, but also required reconstruction of the landslide's basal slip-surface geometry. This reconstruction was necessary because considerable landslide debris remained in the source area at the conclusion of the event (Fig. 5). Three alternative reconstructions yielded source-area volume estimates ranging from $7{\cdot}3 \times 10^6$ $m^3$ to $9{\cdot}2 \times 10^6$ $m^3$, with a mid-range value of $8{\cdot}3 \times 10^6$ $m^3$ deemed most plausible (Iverson *et al.*, 2015). This basal slip surface reconstruction, along with the 2013 lidar topography, also established the initial geometry used in the model simulations presented here.

*Constraints from landslide mobility indices*

Quantitative indices of landslide mobility help place the behaviour of the Oso landslide in context, and also serve as scalar metrics that are useful for comparing the results of the model simulations. The best-known indices of landslide mobility utilise ratios of a landslide's vertical descent $H$ to horizontal extent $L$. One ratio, $H_{max}/L_{max}$, is based on the distances from the top of the landslide headscarp to the most distant point on the landslide deposit (e.g. Corominas, 1996; Legros, 2002). For the Oso landslide, the value $H_{max}/L_{max} = 0{\cdot}105$ applies, indicating an unusually long runout distance for an unchannelised landslide smaller than $10^7$ $m^3$ (Iverson *et al.*, 2015).

Another $H/L$ ratio has deeper physical significance, because it is based on the distances between the centre-of-mass locations in the landslide source area and deposit. Values of this ratio, $H_{CM}/L_{CM}$, thereby serve as proxies for net effective friction coefficients, in which any effects of liquefaction are implicit (e.g. Legros, 2002). Typically values of $H_{CM}/L_{CM}$ are difficult to measure, but at Oso the pre- and post-event lidar topography and source-area slip surface reconstruction allowed $H_{CM}/L_{CM}$ to be determined with high precision. It was found that $H_{CM}/L_{CM} = 0{\cdot}14$ applies, which indicates that the net effective basal friction angle was $\phi_{eff} = \tan^{-1}(H_{CM}/L_{CM}) \approx 8°$. The mobility of the landslide centre of mass is expressed by the reciprocal value $L_{CM}/H_{CM} = 7{\cdot}1$.

Another mobility index gauges landslide spreading behaviour by expressing the total planimetric area $A$ covered by a landslide path as a function of landslide volume $V$. Statistical trends established for diverse, high-speed landslides show that $A \approx 20V^{2/3}$ is typical (Griswold & Iverson, 2008). For the Oso landslide it was found that $A \approx 30V^{2/3}$ applies, indicating that the landslide impacted an area about 50% larger than expected for typical high-speed landslides of similar volume (Iverson *et al.*, 2015). The extensive spreading of the landslide debris at Oso was particularly noteworthy because the landslide began at a site with relatively little potential energy. The crown of the headscarp was only about 180 m higher than the nearly horizontal depositional area on the adjacent river floodplain.

*Numerical results for alternative landslide scenarios at Oso*

The present numerical simulations of the Oso landslide do not attempt to reproduce the details of the three stages of motion described in the previous section. Rather, they focus on landslide behaviour that can be computed by specifying the full source-area geometry in addition to parameter values that satisfy an initial static force balance. Modelled landslide motion is triggered by increasing $p_b/(\rho g_z h)$ uniformly throughout the landslide source area until motion begins at the weakest point, and thereafter $p_b$ evolves as part of the solution of equations (9) through (13). In reporting the numerical results, the time of the first detected motion in the computational domain is designated as $t=0$, but not all of the modelled landslide mass begins to move simultaneously.

Values of all parameters used in the alternative simulations are summarised in Table 1. These values were inferred from laboratory testing of sediment mixtures used in landslide and debris-flow experiments that involved uncompacted materials similar to the predominantly sandy material observed at Oso (Iverson *et al.*, 2000, 2010). No parameter is treated as a freely adjustable fitting coefficient, and most importantly, the intrinsic basal friction angle has a fixed value $\phi=36°$ in every simulation. By contrast, many landslide dynamics studies treat basal friction as an adjustable calibration parameter (e.g. Hungr, 1995; Medina *et al.*, 2008; Lucas *et al.*, 2014).

Normalisation of the governing equations (9) through (13) leads to the inference that landslide behaviour predicted by D-Claw with constant $\phi$ is most sensitive to the values of $m_0-m_{crit}$ and a dimensionless version of $k_0$ (Iverson & George, 2014). This dimensionless version constitutes the timescale ratio $k_0(L_0/g)^{1/2}/\alpha\mu H_0^2$, where $L_0$ is the characteristic landslide length, $H_0$ is the characteristic landslide thickness, $\alpha\mu H_0^2/k_0$ is the timescale for diffusive pore-pressure relaxation and $(L_0/g)^{1/2}$ is the characteristic time over which landslide motion evolves. In the Oso simulations, variations in the value of $k_0$ are the source of nearly all variations in the value of $k_0(L_0/g)^{1/2}/\alpha\mu H_0^2$. Consequently the focus is placed on $k_0$ rather than on its dimensionless analogue. Focus is placed on $m_0$ rather than $m_0-m_{crit}$, because the value $m_{crit}=0{\cdot}64$ is held fixed. Thus, a primary purpose of the alternative simulations is to investigate the sensitivity of model predictions to variations in the values of $m_0$ and $k_0$ when the values of other parameters are constant.

First consider the results of a baseline simulation that provides a good match to the Oso landslide's inferred speed and area of inundation (Fig. 6 and an animation available for viewing (USGS, 2015)). The simulation employs $k_0=10^{-8}\,m^2$ and an initial solid volume fraction $m_0=0{\cdot}62$, which implies that contractive soil deformation occurs during the early stages of landslide motion. Within 30 s of the onset of local slope instability, this contraction leads to widespread liquefaction (Fig. 6), which is accentuated by undrained compression due to fast-moving material exchanging momentum with slower-moving material downslope. As a result, between $t=30$ s and $t=45$ s, the front of the highly mobile landslide propagates at a speed averaging about 30 m/s. As the landslide speed increases, however, the equilibrium solid volume fraction $m_{eq}$ declines, causing contractive behaviour to locally transition into dilative behaviour. This transition occurs most prominently where the landslide is thinnest and fastest, and it reduces pore pressures rapidly. As the modelled landslide moves across the floodplain, its margins, in particular, lose pore pressure and develop increased frictional resistance (see $t=45$ s and $t=60$ s in Fig. 6). Nevertheless, the resistive landslide front is pushed forward by liquefied material behind it, and by $t=60$ s it has travelled across the entire ~1-km-wide floodplain. It subsequently undergoes relatively slow lateral spreading. This modelled behaviour omits any consideration of the Oso landslide's entrainment of river water, but it simulates effects commonly exhibited by liquefied landslides and debris flows that produce lateral levees and distal margins composed of high-friction material (Johnson *et al.*, 2012). In the Oso landslide, as in many debris flows, this high-friction marginal material consisted largely of shattered trees and other woody debris.

Significant variations in landslide mobility are predicted by alternative simulations that use the constant value $k_0=10^{-8}\,m^2$ but use differing values of $m_0$. These variations have a considerable effect on the predicted distributions of landslide deposits (Fig. 7). The model results at $t=600$ s provide a suitable basis for comparing deposits, because in simulations with $m_0<0{\cdot}64$, the landslide total kinetic energy at $t=600$ s is less than 0·01% of its peak value. The case with $m_0=0{\cdot}62$ shows the deposit predicted by the simulation illustrated in Fig. 6. It provides a reasonably good match to the final distribution of deposits observed at Oso (indicated by the outer white line shown in each panel of Fig. 7). Smaller values of $m_0$ produce more extensive deposits, whereas larger values of $m_0$ produce less extensive deposits. The simulation with $m_0=0{\cdot}625$ is noteworthy because it produces a deposit that nearly matches the extent of the 'debris avalanche' portion of the deposit shown in Fig. 5. Thus, if the distal debris flow veneer deposit at Oso was to be excluded, then the simulation with $m_0=0{\cdot}625$ would be preferable to that with $m_0=0{\cdot}62$.

*Landslide energetics in alternative scenarios*

Interpretation of the numerical results is facilitated by computing scalar metrics that summarise landslide energetics for simulations with values of $m_0$ ranging from 0·60 to 0·68 and values of $k_0$ ranging from $1{\cdot}0\times10^{-9}$ to $1{\cdot}0\times10^{-7}\,m^2$. For example, the energy history for the simulated Oso landslide behaviour depicted in Fig. 6 is shown in Fig. 8. To construct

**Table 1. Values of all parameters used in numerical simulations**

| Material property | Best-fit Oso landslide simulation | Alternative simulations |
|---|---|---|
| Basal friction angle, $\phi$: degrees | 36 | 36 |
| Initial solid volume fraction, $m_0$ | 0·62 | 0·60 to 0·68 |
| Lithostatic critical-state solid volume fraction, $m_{crit}$ | 0·64 | 0·64 |
| Initial hydraulic permeability, $k_0$: $m^2$ | $1{\cdot}0\times10^{-8}$ | $1{\cdot}0\times10^{-9}$ to $1{\cdot}0\times10^{-7}$ |
| Pore fluid (muddy water) mass density, $\rho_f$: kg/m$^3$ | 1100 | 1100 |
| Solid grain mass density, $\rho_s$: kg/m$^3$ | 2700 | 2700 |
| Compressibility proportionality coefficient, $a$ | 0·03 | 0·03 |
| Compressibility reference normal stress, $\sigma_0$: Pa | 1000 | 1000 |
| Pore fluid (muddy water) viscosity, $\mu$: Pa s | 0·005 | 0·005 |
| Characteristic grain diameter, $\delta$: m | 0·001 | 0·001 |
| Lateral pressure coefficient, $\kappa$ | 1 | 1 |

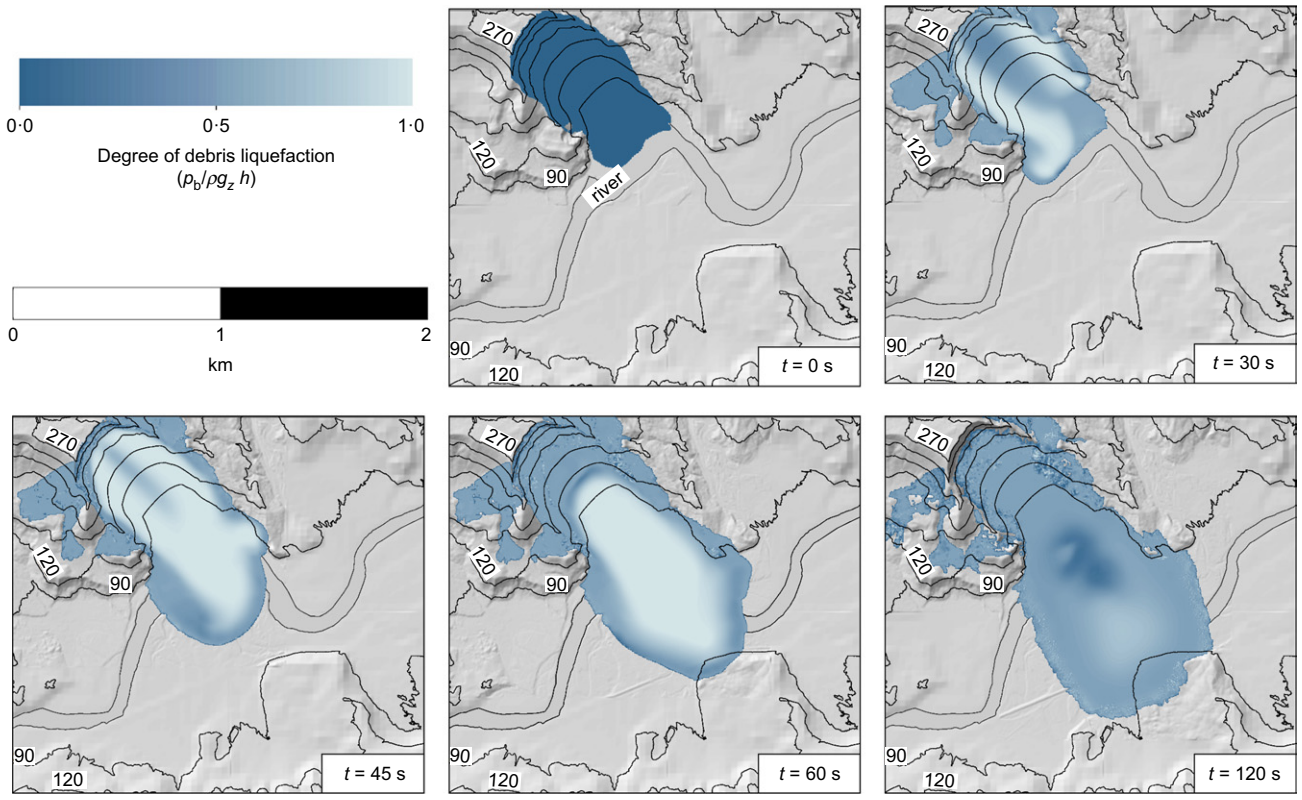


**Fig. 6. Map views of the simulated behaviour of the Oso landslide using the baseline parameter values $m_0 = 0{\cdot}62$ and $k_0 = 10^{-8}$ m$^2$ (the same as values used by Iverson *et al.* (2015)). Landslide area is shown by shading (blue online), with intensity of the shading inversely proportional to the degree of basal liquefaction. Base topography is shown in shaded relief and by topographic contours labelled with elevations in metres**

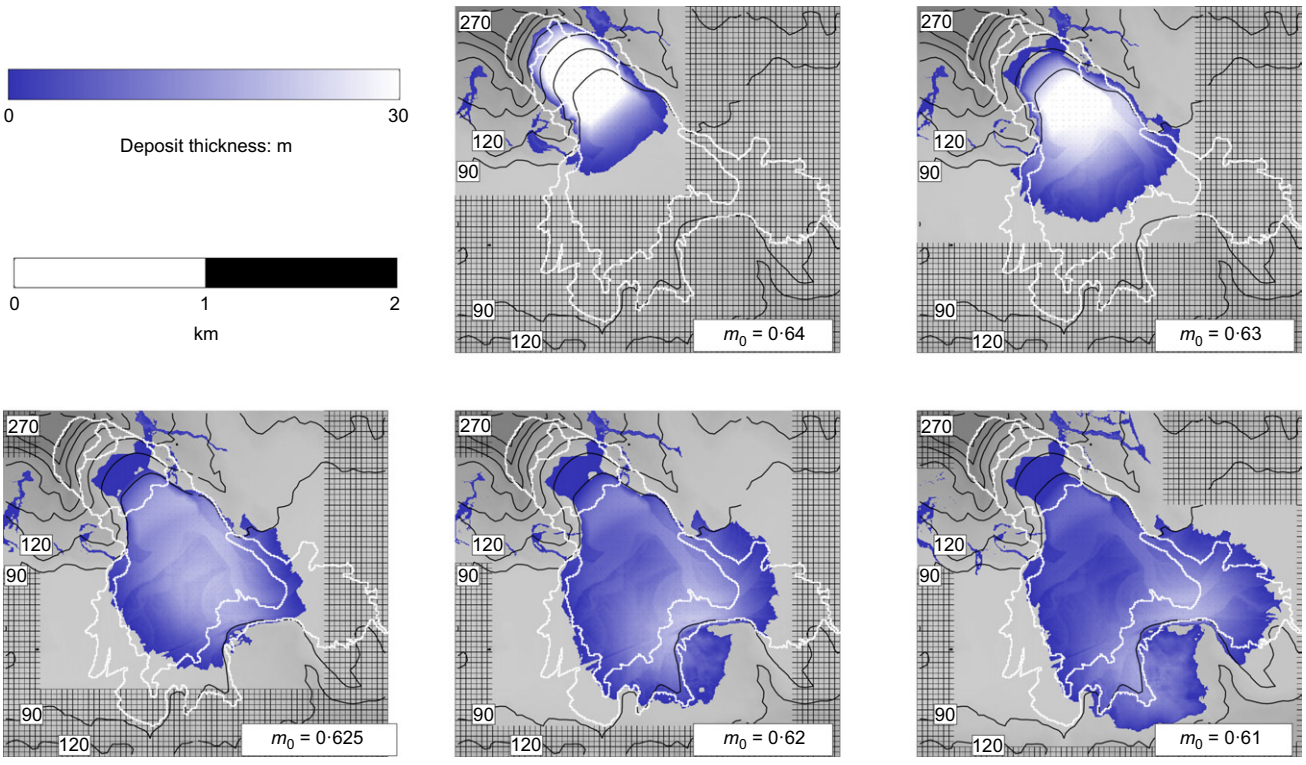


**Fig. 7. Distribution of deposits produced at $t = 600$ s by alternative simulations of landsliding at the Oso site. Simulations use $k_0 = 10^{-8}$ m$^2$, a range of $m_0$ values that are less than or equal to $m_{crit} = 0{\cdot}64$, and hold all other parameter values constant (Table 1). Simulations with $m_0 \geq m_{crit}$ yield results very similar to those with $m_0 = m_{crit}$. White lines correspond to boundaries of landslide depositional units shown in Fig. 5**

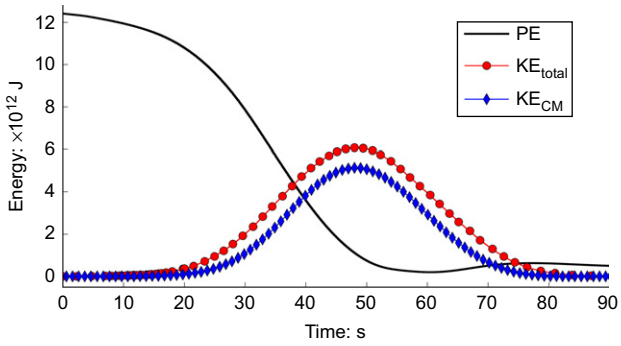


**Fig. 8. Summary of energy evolution during the simulated behaviour of the Oso landslide using the baseline parameter values $m_0 = 0{\cdot}62$ and $k_0 = 10^{-8}$ m$^2$. PE denotes total potential energy, $KE_{total}$ denotes total kinetic energy and $KE_{CM}$ denotes centre-of-mass kinetic energy. PE at $t = 90$ s exceeds PE at $t = 60$ s because some distal debris is pushed onto higher ground adjacent to the southern edge of the floodplain (Fig. 6)**

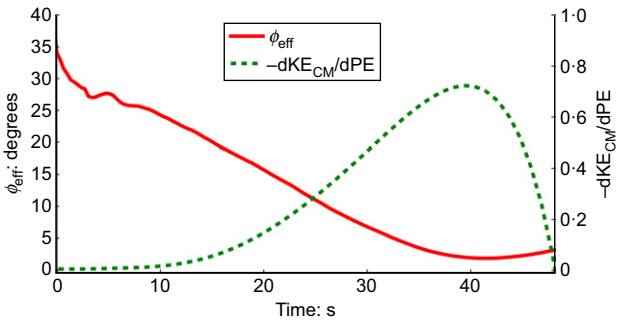


**Fig. 9. Energy conversion efficiency $-dKE_{CM}/dPE$ and effective basal friction angle $\phi_{eff}$ calculated using centre-of-mass motion of the simulated Oso landslide with the baseline parameter values $m_0 = 0{\cdot}62$ and $k_0 = 10^{-8}$ m$^2$. Evolution of $\phi_{eff}$ during $0 < t < 8$ s is not monotonic because it is affected by subtle geometric changes that influence $dH_{CM}/dL_{CM}$ during the first stages of landslide motion**

this history, the initial potential energy ($PE_0$) of the landslide is calculated by using the source-area geometry defined by Iverson *et al.* (2015), a total landslide mass $M = 1{\cdot}73 \times 10^{10}$ kg and an elevation datum fixed at the lowest point in the landslide runout path. Potential energy subsequently evolves as the landslide mass loses elevation during motion. The instantaneous total kinetic energy ($KE_{total}$) of the modelled landslide is calculated by summing the translational kinetic energies of all computational cells, whereas the kinetic energy of the landslide centre of mass ($KE_{CM}$) is calculated from the landslide mass and centre-of-mass translation speed. The differences between these two kinetic energies are due to the spreading of landslide material away from the centre of mass. Nearly half of $PE_0$ of the modelled landslide ($1{\cdot}25 \times 10^{13}$ J) is converted to $KE_{total}$ during the first 48 s of motion, and $KE_{CM}$ represents about 85% of $KE_{total}$ at $t = 48$ s (Fig. 8). Thereafter, both $KE_{CM}$ and $KE_{total}$ decline as the landslide begins to decelerate.

A useful way of viewing the conversion of PE to $KE_{CM}$ during acceleration of the modelled landslide is through analogy with the energetics of a frictional point mass that moves at the velocity of the landslide centre of mass. For a point mass that gains kinetic energy as it descends a slope inclined at the angle $\theta$, the instantaneous energy conversion efficiency expressed by $-dKE_{CM}/dPE$ is related to the instantaneous effective basal friction angle $\phi_{eff}$ by

$$\tan \phi_{eff} = \frac{dH_{CM}}{dL_{CM}} \left(1 + \frac{dKE_{CM}}{dPE}\right) \qquad (19)$$

where $dH_{CM}/dL_{CM} = \tan \theta$ describes the local slope instantaneously descended by the mass (see Appendix). In the presence of 100% energy conversion efficiency, $-dKE_{CM}/dPE = 1$ applies, indicating that $\phi_{eff} = 0$. More generally, however, $\phi_{eff}$ evolves as $-dKE_{CM}/dPE$ and $dH_{CM}/dL_{CM}$ vary along the landslide path.

The coevolution of $-dKE_{CM}/dPE$ and $\phi_{eff}$ calculated by applying equation (19) to the Oso landslide simulation shown in Fig. 6 indicates that the energy conversion efficiency averages about 25% as the landslide centre of mass accelerates, but that the peak energy conversion efficiency exceeds 70% (Fig. 9). This peak efficiency occurs at $t \approx 40$ s, but a continuing decrease of $dH_{CM}/dL_{CM}$ causes the minimum effective basal friction to develop a few seconds later. This minimum value is very small ($\phi_{eff} < 3°$) as a consequence of a high degree of transient liquefaction (e.g. at $t = 45$ s in Fig. 6). Effective friction subsequently increases, followed by deceleration of the landslide centre of mass beginning at $t = 48$ s. (After $t = 48$ s, $KE_{CM}$ declines, and equation (19) is no longer valid.) A key aspect of the evolution of effective friction shown in Fig. 9 is that it is predicted, rather than specified, by the model. Other landslide dynamics models commonly specify an evolution of effective friction in order to fit observations (e.g. Lucas *et al.*, 2014).

The evolution of total kinetic energy depends strongly on values of $m_0$ and $k_0$ used in alternative simulations. When $k_0 = 10^{-8}$ m$^2$ is held constant, both the peak kinetic energy and the kinetic energy growth rate decline systematically as the value of $m_0$ increases from 0·62 to the lithostatic critical-state value $m_0 = m_{crit} = 0{\cdot}64$ (Fig. 10). This behaviour is a clear consequence of a reduced propensity for sediment contraction and liquefaction during landslide motion.

More complicated variations in kinetic energy evolution are evident in simulations that hold $m_0 = 0{\cdot}62$ constant but use differing values of $k_0$ (Fig. 11). Changing the permeability from the baseline value $k_0 = 10^{-8}$ m$^2$ to the larger value $k_0 = 10^{-7}$ m$^2$ causes the modelled landslide to initially gain kinetic energy at an increased rate, but to subsequently lose energy more rapidly. These relatively rapid gains and losses of kinetic energy are a consequence of the effect of $k$ on the timescale for pore-pressure response, $\alpha\mu h^2/3k$, which appears in equation (13). When this timescale is sufficiently small, pore pressure can be generated rapidly by contractive deformation, but excess pore pressure also dissipates rapidly after contraction ceases. Therefore, the modelled landslide with $k_0 = 10^{-7}$ m$^2$ exhibits only moderate net mobility in comparison to the modelled Oso landslide with $k_0 = 10^{-8}$ m$^2$. By contrast, if the value of $k_0$ is reduced from $10^{-8}$ m$^2$ to

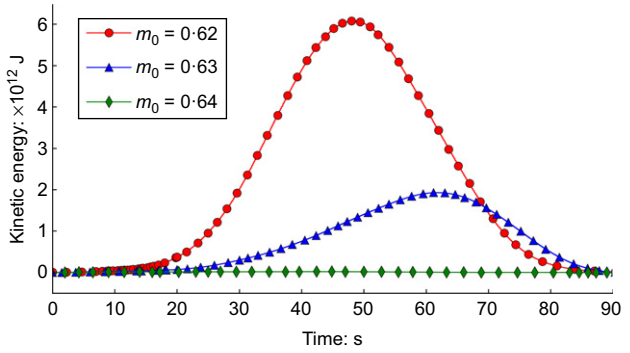


**Fig. 10. Evolution of total kinetic energy in alternative Oso landslide simulations that employ the baseline value $k_0 = 10^{-8}$ m$^2$ and varying values of $m_0$. Non-zero kinetic energy develops with $m_0 = 0{\cdot}64$ but is not visible on this scale**

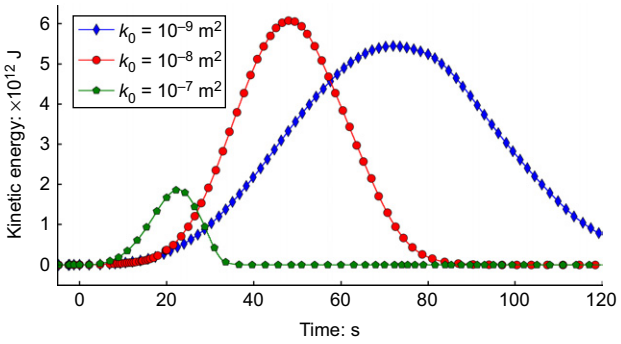


**Fig. 11. Evolution of total kinetic energy in alternative Oso landslide simulations that employ the baseline value $m_0 = 0{\cdot}62$ and varying values of $k_0$**

$10^{-9}$ m$^2$, the landslide accelerates more slowly and gains kinetic energy at a reduced rate, because liquefaction is initially retarded by low permeability (Fig. 11). Liquefaction eventually becomes more pervasive and persistent than in the baseline case with $k_0 = 10^{-8}$ m$^2$, however. Therefore, the modelled landslide with $k_0 = 10^{-9}$ m$^2$ ultimately exhibits increased runout, despite the fact that its peak kinetic energy is smaller than that of the landslide with $k_0 = 10^{-8}$ m$^2$.

*Landslide mobility indices for alternative scenarios*

Clear trends emerge when scalar indices of landslide mobility are calculated from the results of alternative simulations that use values of $m_0$ ranging from 0·60 to 0·68 and values of $k_0$ ranging from $10^{-9}$ to $10^{-7}$ m$^2$. One mobility index gauges the landslide energy conversion efficiency by dividing the peak total kinetic energy $KE_{max}$ by the initial landslide potential energy, $PE_0$. A graph of $KE_{max}/PE_0$ as a function of $m_0$ and $k_0$ shows that, irrespective of the value of $k_0$, the energy conversion efficiency is universally $< 0{\cdot}04$ if $m_0 \geq m_{crit}$, but it increases systematically and roughly in proportion to $m_{crit} - m_0$ if $m_0 < m_{crit}$ (Fig. 12). Thus, as a result of a transition in the propensity for landslide liquefaction, a behavioural bifurcation separating slow landslide motion from runaway, high-speed motion occurs at $m_0 = m_{crit}$. However, the bifurcation becomes more muted as $k_0$ increases, as would be expected from the results shown in Fig. 11. Also consistent with those results is a trend showing that $KE_{max}/PE_0$ has little to no dependence on $k_0$ if $k_0 \leq 10^{-8}$ m$^2$. This behaviour arises from the effect of low permeability in retarding the early stages of landslide liquefaction and acceleration.

The same set of simulations summarised in Fig. 12 yields centre-of-mass mobility indices $L_{CM}/H_{CM}$ that range from less than 3 to more than 15 for contractive cases with $m_0 < m_{crit}$ (Fig. 13). The empirically determined value for the Oso landslide was $L_{CM}/H_{CM} = 7{\cdot}1$, and no simulation presented here yields this precise value. However, Fig. 13 shows that tuning the values of $m_0$ and $k_0$ could easily yield an exact match to $L_{CM}/H_{CM} = 7{\cdot}1$, if that were desirable. More importantly, computed values of $L_{CM}/H_{CM}$ increase monotonically as $m_{crit} - m_0$ increases and as $k_0$ decreases. Thus, the effect of low permeability in causing persistent liquefaction that enhances runout is evident in the mobility index $L_{CM}/H_{CM}$ – despite the fact that low permeability initially retards liquefaction and landslide acceleration (Fig. 11 and Fig. 12). Like the index $KE_{max}/PE_0$, the index $L_{CM}/H_{CM}$ demonstrates a mobility bifurcation at $m_0 = m_{crit}$. Moreover, the bifurcation becomes muted as the value of $k_0$ increases. Finally, it is noted that Fig. 13 lacks data points for $k_0 = 10^{-9}$ m$^2$ and $m_0 < 0{\cdot}62$. No final deposit geometries were computed for such cases because the simulated landslides were so mobile that they left the computational domain.

The simulations also yield values of the mobility index $A/V^{2/3}$, which provides a measure of the area inundated during landslide spreading. Simulations for contractive cases with $m_0 < m_{crit}$ yield values of $A/V^{2/3}$ ranging from about 10 to about 50, whereas all simulations for dilative cases with $m_0 > m_{crit}$ yield $A/V^{2/3} \approx 10$ (Fig. 14). The observed value for the Oso landslide is $A/V^{2/3} \approx 30$. Again, no exact match is provided by any of these simulations, but the trends evident in Fig. 14 provide strong evidence that the value $k_0 = 10^{-8}$ m$^2$ provides better predictions of inundation areas than do the alternative values $k_0 = 10^{-7}$ m$^2$ or $k_0 = 10^{-9}$ m$^2$. Details of computed inundation areas for simulations with $k_0 = 10^{-8}$ m$^2$ are shown in Fig. 7.

## CONCLUSIONS

The dynamics of the disastrous Oso landslide of 22 March 2014 can be analysed by using a recently developed depth-integrated computational model, called D-Claw. The model simulates landslide motion that begins when a statically balanced initial state is perturbed by gradually increasing basal pore-water pressure. Following onset of motion, effective landslide friction evolves as a consequence of coupled evolution of the depth-integrated solid volume fraction and basal pore pressure.

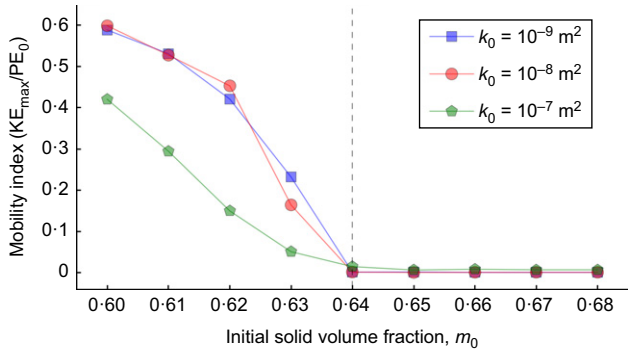


**Fig. 12. Landslide mobility index $KE_{max}/PE_0$ expressing peak total kinetic energy divided by initial potential energy in alternative Oso landslide simulations, which employ a range of $m_0$ and $k_0$ values. Dashed line designates the bifurcation value $m_0 = m_{crit} = 0{\cdot}64$. Values of $KE_{max}/PE_0$ are non-zero in every case but are universally small for $m_0 > m_{crit}$**

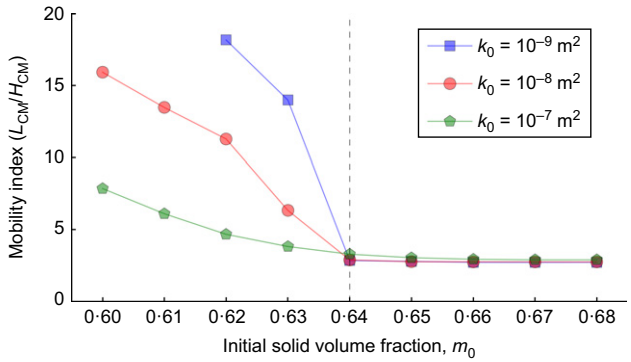


**Fig. 13. Landslide mobility index $L_{CM}/H_{CM}$ expressing total translation of centre of mass computed in alternative Oso landslide simulations, which employ a range of $m_0$ and $k_0$ values. Dashed line designates the bifurcation value $m_0 = m_{crit} = 0{\cdot}64$**

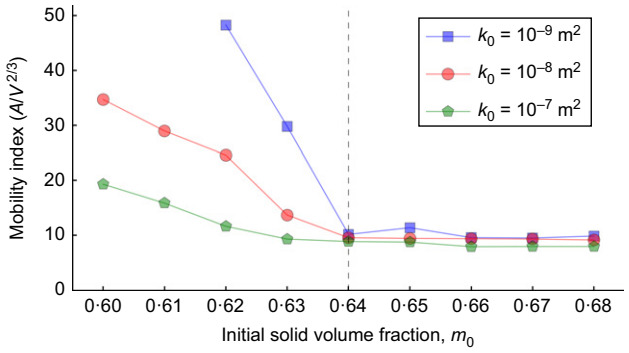


**Fig. 14. Landslide mobility index $A/V^{2/3}$ expressing area of landslide path computed in alternative Oso landslide simulations, which employ a range of $m_0$ and $k_0$ values and hold $V = 8{\cdot}3 \times 10^6$ m$^3$ constant. Dashed line designates the bifurcation value $m_0 = m_{crit} = 0{\cdot}64$**

A suite of alternative simulations of the Oso event uses a fixed basal slip-surface geometry as well as fixed values of the basal friction angle $\phi = 36°$ and lithostatic critical-state solid volume fraction $m_{crit} = 0{\cdot}64$. The simulations show that pore-pressure feedback may or may not lead to widespread liquefaction and high landslide mobility, contingent mostly on the difference between $m_{crit}$ and the initial solid volume fraction, $m_0$. A landslide mobility bifurcation consequently arises due to differences between initial soil conditions that favour contractive behaviour and positive pore-pressure feedback (with $m_0 < m_{crit}$), and those that favour dilative behaviour and negative pore-pressure feedback (with $m_0 > m_{crit}$). The bifurcation is muted by increasing the value of the initial hydraulic permeability, $k_0$.

A D-Claw simulation that fits the inferred event duration and mapped inundation area of the Oso landslide reasonably well utilises $m_0 = 0{\cdot}62$ and $k_0 = 10^{-8}$ m$^2$, implying that slightly contractive shear behaviour and moderate permeability influence the early stages of landslide motion. This simulation predicts that widespread liquefaction develops over the course of about 30 s following the onset of local slope instability at $t = 0$. During the ensuing landslide runout, liquefaction causes the landslide front to advance at speeds reaching 30 m/s, causes the conversion of potential energy to kinetic energy to peak at an efficiency $> 70\%$, and causes the instantaneous effective basal friction angle to reach a minimum value $\phi_{eff} < 3°$ at $t \approx 42$ s. Deceleration of the landslide centre of mass begins 6 s later, but advance of the landslide's distal margin continues until it is impeded by topographic obstructions. As a result, the modelled landslide crosses the 1-km breadth of the adjacent river floodplain in about 60 s.

Alternative simulations reveal the sensitivity of modelled landslide behaviour to the values of $m_0$ and $k_0$. Three landslide mobility indices demonstrate this sensitivity by summarising results of simulations in which values of $m_0$ range from 0·6 to 0·68 and values of $k_0$ range from $10^{-9}$ to $10^{-7}$ m$^2$. The indices gauge the conversion of gravitational potential energy to peak kinetic energy ($KE_{max}/PE_0$), the normalised distance of translation of the landslide centre of mass ($L_{CM}/H_{CM}$), and the normalised planimetric area impacted by the landslide ($A/V^{2/3}$). For simulations with $m_0 \geq m_{crit}$, all indices show that landslide mobility is quite limited and is nearly invariant. These modelled landslides travel only about 100 m before stopping. By contrast, for simulations with $m_0 < m_{crit}$, landslide mobility increases dramatically as $m_0$ decreases, with a bifurcation in mobility at $m_0 = m_{crit}$. For values $k_0 \leq 10^{-8}$ m$^2$, the bifurcation is quite sharp, but for $k_0 = 10^{-7}$ m$^2$ it is more subdued. This muting of the bifurcation is a consequence of the reduced efficacy of liquefaction that occurs when permeability is large enough to allow rapid pore-pressure relaxation.

An important practical implication of these findings is that large differences in landside mobility can result from small differences in initial conditions. Model studies aimed at landslide hazard prognostication can in principle account for the associated uncertainties by adopting probabilistic methods. Nevertheless, the challenge in making useful predictions is great, because bifurcating landslide dynamics can result in divergent outcomes.

## APPENDIX. RELATION BETWEEN BASAL FRICTION AND ENERGY CONVERSION FOR A TRANSLATING POINT MASS

The momentum-conservation equation for a rigid frictional body of mass $M$ descending a slope inclined at the angle $\theta$ is

$$M\frac{du}{dt} = Mg(\sin\theta - \cos\theta\tan\phi) \tag{20}$$

where $\phi$ is the basal friction angle and $u$ is the velocity parallel to the slope. The rates of change of the potential energy (PE) and kinetic energy (KE) of the mass during this motion are given by

$$\frac{dPE}{dt} = Mg\frac{dz}{dt} = Mgu_z \tag{21}$$

and

$$\frac{dKE}{dt} = \frac{1}{2}M\frac{du^2}{dt} = Mu\frac{du}{dt} \tag{22}$$

where $z$ is the vertical coordinate of the mass, $u_z = dz/dt$ is the vertical component of $u$, and downward motion implies that $u_z < 0$. Equations (21) and (22) may be combined to obtain

$$\frac{dKE}{dPE} = \frac{u}{u_z}\frac{du/dt}{g} \tag{23}$$

Because $u_z < 0$, equation (23) indicates that $dKE/dPE < 0$ if $du/dt > 0$. This result reflects the simultaneous growth of kinetic energy and loss of potential energy as the mass accelerates downslope. By multiplying each term of equation (20) by $u/Mg$ and then employing the substitution $u\sin\theta = -u_z$, equation (20) can be reduced to

$$\frac{\tan\phi}{\tan\theta} - 1 = \frac{u}{u_z}\frac{du/dt}{g} \tag{24}$$

Combination of equations (23) and (24) then yields

$$\tan\phi = \tan\theta\left(1 + \frac{dKE}{dPE}\right) \tag{25}$$

Finally, if the local angle of the slope is expressed as $\tan\theta = dH_{CM}/dL_{CM}$, then equation (25) can be written as

$$\tan\phi = \frac{dH_{CM}}{dL_{CM}}\left(1 + \frac{dKE}{dPE}\right) \tag{26}$$

This equation relates the effective basal friction coefficient $\tan\phi$ to the energy-conversion efficiency $-dKE/dPE$ during infinitesimal displacements with vertical and horizontal components given by $dH_{CM}$ and $dL_{CM}$.

## ACKNOWLEDGEMENTS

The authors would like to thank Mark Reid and two anonymous reviewers for helpful critiques of the manuscript. They also especially thank their many USGS colleagues, as well as state of Washington and Snohomish County staff, who participated in the response to the Oso landslide disaster.

## NOTATION

$A$ planimetric area of landslide path
$a$ dimensionless coefficient in compressibility equation

$b$ elevation of landslide base
$D$ depth-integrated granular dilation rate
$e$ void ratio
$g$ magnitude of gravitational acceleration vector
$g_x$, $g_y$, $g_z$ Cartesian components of gravitational acceleration vector
$H_{CM}$ vertical height traversed by landslide centre of mass
$H_{max}$ total vertical height encompassed by landslide path
$h$ landslide thickness in $z$ direction
$K$ hydraulic conductivity
$KE_{CM}$ landslide centre-of-mass kinetic energy
$KE_{max}$ landslide peak kinetic energy
$KE_{total}$ landslide total kinetic energy
$k$ intrinsic hydraulic permeability
$k_0$ initial value of $k$
$L$ landslide length
$L_{CM}$ horizontal distance traversed by landslide centre of mass
$L_{max}$ total horizontal distance encompassed by landslide path
$M$ landslide mass
$m$ solid volume fraction ($=1-n=1/(1+e)$)
$m_{crit}$ lithostatic critical-state value of $m$
$m_{eq}$ dynamic equilibrium value of $m$
$m_0$ initial value of $m$
$N$ dimensionless state parameter
$n$ porosity
PE landslide gravitational potential energy
$PE_0$ initial value of PE
$p$ pore-fluid pressure
$p_b$ basal pore-fluid pressure
$p_e$ excess pore-fluid pressure (i.e. deviation from hydrostatic pressure)
$\boldsymbol{q}$ specific discharge of pore fluid
$q_z$ $z$ component of $\boldsymbol{q}$
$t$ time
$u$, $v$, $w$ Cartesian components of $\boldsymbol{v}$ in the $x$, $y$ and $z$ directions, respectively
$V$ landslide volume
$\boldsymbol{v}$ velocity of solid–fluid mixture
$\boldsymbol{v}_f$ velocity of pore-fluid phase
$\boldsymbol{v}_s$ velocity of granular solid phase
$x$, $y$, $z$ orthogonal Cartesian coordinates, with $z$ positive upward
$\alpha$ bulk compressibility of solid–fluid mixture
$\dot{\gamma}$ shear rate of solid–fluid mixture
$\delta$ characteristic grain diameter
$\eta$ elevation of landslide surface
$\kappa$ lateral pressure coefficient
$\mu$ dynamic viscosity of pore fluid
$\theta$ slope angle
$\rho$ bulk density of solid–fluid mixture
$\rho_f$ mass density of pore fluid
$\rho_s$ mass density of solid grains
$\sigma_e$ effective normal stress
$\sigma_0$ reference value of normal stress
$\phi$ constant-volume basal friction angle
$\phi_{eff}$ effective basal friction angle
$\psi$ dilatancy angle

## REFERENCES


Bagnold, R. A. (1954). Experiments on a gravity-free dispersion of large solid spheres in a Newtonian fluid under shear. *Proc. R. Soc. London, Ser. A* **225**, No. 1160, 49–63.

Bale, D. S., LeVeque, R. J., Mitran, S. & Rossmanith, J. A. (2002). A wave propagation method for conservation laws and balance laws with spatially varying flux functions. *SIAM J. Sci. Comput.* **24**, No. 3, 955–978.

Bear, J. (1972). *Dynamics of fluids in porous media*. New York, NY, USA: Dover.

Bishop, A. W. (1973). The stability of tips and spoil heaps. *Q. J. Engng Geol. Hydrogeol.* **6**, No. 3–4, 335–376.

Boyer, F., Guazzelli, E. & Pouliquen, O. (2011). Unifying suspension and granular rheology. *Phys. Rev. Lett.* **107**, No. 18, 188301, http://dx.doi.org/10.1103/PhysRevLett.107.188301.

Clawpack (2015) See http://www.clawpack.org (accessed 22/08/2015).

Corominas, J. (1996). The angle of reach as a mobility index for small and large landslides. *Can. Geotech. J.* **33**, No. 2, 260–271.

Dragovich, J. D., Stanton, B. W., Lingley, W. S., Griesel, G. A. & Polenz, M. (2003). *Geologic map of the Mount Higgins 7.5 minute quadrangle, Skagit and Snohomish Counties, Washington*, Open File Report 2003-12. Olympia, WA, USA: Washington State Division of Geology and Earth Resources.

Eckersley, D. (1990). Instrumented laboratory flowslides. *Géotechnique* **40**, No. 3, 489–502, http://dx.doi.org/10.1680/geot.1990.40.3.489.

Freeze, R. A. & Cherry, J. A. (1979). *Groundwater*. Englewood Cliffs, NJ, USA: Prentice-Hall.

George, D. L. (2008). Augmented Riemann solvers for the shallow water equations over variable topography with steady states and inundation. *J. Computat. Phys.* **227**, No. 6, 3089–3113.

George, D. L. & Iverson, R. M. (2014). A depth-averaged debris-flow model that includes the effects of evolving dilatancy. II. numerical predictions and experimental tests. *Proc. R. Soc. London, Ser. A* **470**, No. 2170, 20130820, http://dx.doi.org/10.1098/rspa.2013.0820.

Gray, J. M. N. T., Wieland, M. & Hutter, K. (1999). Gravity-driven free surface flow of granular avalanches over complex basal topography. *Proc. R. Soc. London, Ser. A* **455**, No. 1985, 1841–1874.

Gray, J. M. N. T., Tai, Y-C. & Noelle, S. (2003). Shock waves, dead zones and particle-free regions in rapid granular free-surface flows. *J. Fluid Mech.* **491**, 161–181.

Griswold, J. P. & Iverson, R. M. (2008). *Mobility statistics and automated hazard mapping for debris flows and rock avalanches*, U.S. Geological Survey Scientific Investigations Report 2007-5276. Reston, VA, USA: U.S. Geological Survey. See http://pubs.usgs.gov/sir/2007/5276/ (accessed 03/09/2015).

Hungr, O. (1995). A model for the runout analysis of rapid flow slides, debris flows, and avalanches. *Can. Geotech. J.* **32**, No. 4, 610–623.

Hungr, O. & Evans, S. G. (2004). Entrainment of debris in rock avalanches: an analysis of the long-runout mechanism. *Geol. Soc. Amer. Bull.* **116**, No. 9–10, 1240–1252.

Hutchinson, J. N. & Bhandari, R. K. (1971). Undrained loading, a fundamental mechanism of mudflows and other mass movements. *Géotechnique* **21**, No. 4, 353–358, http://dx.doi.org/10.1680/geot.1971.21.4.353.

Iverson, R. M. (2003). The debris-flow rheology myth. In *Debris-flow hazards mitigation: mechanics, prediction, and assessment* (eds C. L. Chen and D. Rickenmann), vol. 1, pp. 303–314. Rotterdam, the Netherlands: Millpress.

Iverson, R. M. (2005). Regulation of landslide motion by dilatancy and pore-pressure feedback. *J. Geophys. Res. – Earth Surface* **110**, No. F2, F02015, http://dx.doi.org/10.1029/2004JF000268.

Iverson, R. M. & Denlinger, R. P. (2001). Flow of variably fluidized granular masses across three-dimensional terrain: 1. Coulomb mixture theory. *J. Geophys. Res.* **106**, No. B1, 537–552.

Iverson, R. M. & George, D. L. (2014). A depth-averaged debris-flow model that includes the effects of evolving dilatancy. I. physical basis. *Proc. R. Soc. London, Ser. A* **470**, No. 2170, 20130819, http://dx.doi.org/10.1098/rspa.2013.0819.

Iverson, R. M. & Ouyang, C. (2015). Entrainment of bed material by Earth-surface mass flows: review and reformulation of depth-integrated theory. *Rev. Geophys.* **53**, No. 1, 27–58, http://dx.doi.org/10.1002/2013RG000447.

Iverson, R. M., Reid, M. E. & LaHusen, R. G. (1997). Debris-flow mobilization from landslides. *Ann. Rev. Earth Planetary Sci.* **25**, No. 1, 85–138.

Iverson, R. M., Reid, M. E., Iverson, N. R., LaHusen, R. G., Logan, M., Mann, J. E. & Brien, D. L. (2000). Acute sensitivity of landslide rates to initial soil porosity. *Science* **290**, No. 5491, 513–516.

Iverson, R. M., Logan, M., LaHusen, R. G. & Berti, M. (2010). The perfect debris flow? Aggregated results from 28 large-scale experiments. *J. Geophys. Res. – Earth Surface* **115**, No. F3, F03005, http://dx.doi.org/10.1029/2009JF001514.

Iverson, R. M., Reid, M. E., Logan, M., LaHusen, R. G., Godt, J. W. & Griswold, J. G. (2011). Positive feedback and momentum growth during debris-flow entrainment of wet bed sediment.

*Nature Geosci.* **4**, No. 2, 116–121, http://dx.doi.org/10.1038/NGEO1040.

Iverson, R. M., George, D. L., Allstadt, K., Reid, M. E., Collins, B. D., Vallance, J. W., Schilling, S. P., Godt, J. W., Cannon, C. M., Magirl, C. S., Baum, R. L., Coe, J. A., Schulz, W. H. & Bower, J. B. (2015). Landslide mobility and hazards: implications of the 2014 Oso disaster. *Earth Planetary Sci. Lett.* **420**, 197–208, http://dx.doi.org/10.1016/j.epsl.2014.12.020.

Jibson, R. W. (1992). The Mameyes, Puerto Rico landslide disaster of October 7, 1985. *Landslides/Landslide Mitigation. Geol. Soc. Am. Rev. Engng Geol.* **IX**, 37–54.

Johnson, C. G., Kokelaar, B. P., Iverson, R. M., Logan, M., LaHusen, R. G. & Gray, J. M. N. T. (2012). Grain-size segregation and levee formation in geophysical mass flows. *J. Geophys. Res. – Earth Surface* **117**, No. F1, F01032, http://dx.doi.org/10.1029/2011JF002185.

Legros, F. (2002). The mobility of long-runout landslides. *Engng Geol.* **63**, No. 3–4, 301–331.

LeVeque, R. J. (2002). *Finite volume methods for hyperbolic problems*. Cambridge, UK: Cambridge University Press.

LeVeque, R. J., George, D. L. & Berger, M. J. (2011). Tsunami modeling with adaptively refined finite volume methods. *Acta Numerica* **20**, 211–289.

Lucas, A., Mangeney, A. & Ampuero, J. P. (2014). Frictional velocity-weakening in landslides on Earth and on other planetary bodies. *Nature Communs* **5**, 3417, http://dx.doi.org/10.1038/ncomms4417.

McDougall, S. & Hungr, O. (2004). A model for the analysis of rapid landslide motion across three-dimensional terrain. *Can. Geotech. J.* **41**, No. 6, 1084–1097.

Medina, V., Hürlimann, M. & Bateman, A. (2008). Application of FLATmodel, a 2D finite volume code, to debris flows in the northeastern part of the Iberian Peninsula. *Landslides* **5**, No. 1, 127–142.

Ochiai, H., Sammori, T. & Okada, Y. (2007). Landslide experiments on artificial and natural slopes. In *Progress in landslide science* (eds K. Sassa, H. Fukuoka, F. Wang and G. Wang), pp. 209–226. Berlin, Germany: Springer.

Pitman, E. B. & Le, L. (2005). A two-fluid model for avalanche and debris flows. *Phil. Trans. R. Soc., Ser. A* **363**, No. 1832, 1573–1601.

Savage, S. B. & Hutter, K. (1989). The motion of a finite mass of granular material down a rough incline. *J. Fluid Mech.* **199**, 177–215.

Schofield, A. N. & Wroth, C. P. (1968). *Critical state soil mechanics*. New York, NY, USA: McGraw-Hill.

Spence, K. J. & Guymer, I. (1997). Small-scale laboratory flowslides. *Géotechnique* **47**, No. 5, 915–932, http://dx.doi.org/10.1680/geot.1997.47.5.915.

USGS (2015) See http://volcanoes.usgs.gov/vsc/movies/movie_98/landslide_simulations.mp4 (accessed 21/08/2015).

Wang, G. & Sassa, K. (2001). Factors affecting rainfall-induced flowslides in laboratory flume tests. *Géotechnique* **51**, No. 7, 587–599, http://dx.doi.org/10.1680/geot.2001.51.7.587.

Wang, G. & Sassa, K. (2003). Pore-pressure generation and movement of rainfall-induced landslides: effects of grain size and fine-particle content. *Engng Geol.* **69**, No. 1, 109–125.

Wood, D. M. (1990). *Soil behavior and critical state soil mechanics*. Cambridge, UK: Cambridge University Press.